Early Stages of Crystallization in Isotactic Polypropylene

E. L. Heeley,*,† A. V. Maidens,‡ P. D. Olmsted,‡ W. Bras,§ I. P. Dolbnya,§ J. P. A. Fairclough,† N. J. Terrill,⊥ and A. J. Ryan*,†

The Polymer Centre, Department of Chemistry, University of Sheffield, Sheffield, S3 7HF, UK; Department of Physics & Astronomy and Polymer IRC, University of Leeds, Leeds LS2 9JT, UK; Netherlands Organization for Scientific Research (NWO), DUBBLE-CRG/ESRF, B.P. 220, F-38043 Grenoble Cedex, France; and CLRC, Daresbury Laboratory, Daresbury, Warrington, Cheshire, WA4 4AD, UK

Received August 22, 2002; Revised Manuscript Received February 12, 2003

ABSTRACT: An experimental study of the early stages of crystallization in iPP has shown a qualitative difference between the behavior at low supercooling with that observed with a deep quench. To address previous misgivings in the limits of resolution of crystallites by wide-angle scattering, a new detector has been used that has many orders of magnitude improvements in count rate. At low degrees of undercooling there is a substantial gap between the appearance of a peak in the small-angle scattering, associated with electron density modulations, and the resolution of crystallites. This early growth in electron density has been analyzed in terms of a spinodal decomposition process and the stability limit of isotactic polypropylene determined for three different samples of varying molecular weight. The underlying physics of the early stages of crystallization are discussed and a number of scenarios eliminated; at high temperature Avrami kinetics are not observed whereas at low temperatures the structure in both the small-angle and wide-angle regimes grow contemporaneously following secondary nucleation.

Introduction

Recent work on polymer crystallization has given considerable attention to the possibility that the crystal phase in the final semicrystalline state could be preceded by transient liquid phases of different density to that of the initial quenched bulk isotropic melt or annealed glassy state. Time-resolved small-angle X-ray scattering (SAXS) shows the development of scattering intensity, indicating the growth of structure at length scales corresponding to the long period of the final semicrystalline material, significantly preceding the appearance of Bragg peaks that can be attributed to crystals in the wide-angle X-ray scattering (WAXS). Spinodal kinetics have been reported in a number of polymeric materials using a variety of techniques: Imai and co-workers investigated cold crystallized (annealed from the glassy state) poly(ethylene terephthalate) (PET) using time-resolved SAXS and WAXS;[1−4] Matsuba and Kaji and co-workers examined cold crystallized isotactic and sydiotactic polystyrene (iPS and sPS), using Fourier transform infrared spectroscopy (FTIR) and depolarized light scattering (DPLS),[5−6] and also cold crystallized poly(ethylene naphthalate) (PEN), using SAXS,[7] and fitted their kinetics data with a Cahn−Hilliard law at early times and Furakawa scaling at later times. Ezquerra et al.[8] reported spinodal behavior in cold crystallized poly(ether ketone ketone) (PEKK). We have previously observed spinodal behavior in melt crystallized iPP[9,10] and with Olmsted et al.[11] interpreted the SAXS intensity for the transient liquid phase in terms of spinodal-type kinetics by analogy with Cahn−Hilliard theory.[12,13] Most recently, Balta-Calleja and co-workers[14] have observed spinodal kinetics in melt crystallized nylon.

Various studies have suggested that the denser transient phase involves chain orientation. SAXS experiments carried out by Blundell et al. on extension-induced crystallization of PET and PEN indicate that the strain provides molecular orientation that speeds up crystallization but that crystallization only takes place after the strain is released, allowing the chains to relax into crystalline order.[15,16] In this case the precursor mesophase takes the form of a transient smectic liquid crystal phase. Crystallization from oriented states shows a low activation energy, suggesting a process driven by local segmental activity rather than whole chain reptation. However, Blundell et al. noted that these studies are insufficient to unambiguously differentiate between the existence of a mesophase and extended linear chains of random monomeric sequence without any long-ranged correlation, although they speculated that a mesophase might form a state intermediate between extended random chains and the final crystalline state.

Investigations[6,17,18] of the chain conformation suggest that the transformation to a denser, oriented transient phase is associated with conformational changes, which may be understood either as transforming randomly coiled molecules into stiffer chains with rodlike sections or increasing the mean molecular stiffness (or persistence length). Matsuba et al. have measured orientation fluctuations in iPS and sPS finding[6] increasing trans-conformation bands during the induction period prior to the emergence of crystalline order using FTIR, suggesting that the emergence of stiffer, rodlike sections leading to an oriented liquid state is driven by conformational change at the molecular level. Tashiro et al.[17,18] studied a similar mechanism in the case of conformationally disordered (CONDIS) states in the hexagonal phase of PE crystallized from the melt, using SAXS, IR, and Raman spectroscopy. They observed a

† University of Sheffield.
‡ University of Leeds.
§ Netherlands Organization for Scientific Research.
⊥ Daresbury Laboratory.
* Corresponding authors: e-mail e.heeley@shef.ac.uk or a.ryan@shef.ac.uk.

10.1021/ma021373i CCC: $25.00
Published on Web 04/24/2003

hexagonal phase as a transient phase before the formation of orthorhombic crystals. This phase exhibited gauche defects along the chain, and its role as a route to crystallization was speculated with a CONDIS phase being seen both in rapid quenches and on slower cooling. It was noted that the hexagonal phase is most likely metastable at atmospheric pressure, though there is no evidence for spinodal behavior in this particular system.[19] Huang et al.[20] used NMR and DSC (differential scanning calorimetry) to observe conformation changes in amorphous PET annealed above its glass transition temperature. An increase in trans content near the onset of crystallization was analyzed with a three-domain model of crystalline (all-trans), constrained noncrystalline (trans-rich), and amorphous (gauche-rich) states. Gauche-to-trans conversion was assumed to proceed before subsequent crystallization, with the trans-rich conformers regarded as precursors for PET crystallization.

Ezquerra et al.[8] and Imai et al.[1−3,5−7] have used the Doi−Onsager model[21] for the critical concentration of rods in solution above which one would expect to see nematic ordering, making the assumption that stiffening and alignment should occur before intermolecular forces eventually drive crystallization. In this model an isotropic liquid becomes unstable at a critical concentration $C^* \propto 1/L$, where L is the length of the "rod", taken in the melt case to be proportional to the chain persistence length. Upon stiffening the polymer by, for example, increasing trans-bond content (or more generally the preferred low-temperature sequence), the length and fraction of stiff segments increase, which would then lead to a critical length L_{p^*} above which the isotropic liquid becomes unstable. Matsuba et al.[5,6] fit their data to a critical length of about five alternate trans and gauche (TG) conformers in iPS (i.e., 10 monomer units)[5] and 10 TT sequences in sPS.[6] They note that the Doi model applies to stiff polymers and thus should not apply to a flexible chain like sPS but speculate that conformational changes along the chain may lead to increase in effective segment length.[6]

Olmsted et al.[11] have taken this suggestion further and noted that there is generally expected to be a coupling between local conformational order and density. There is an obvious coupling through the Doi−Onsager formulation of liquid crystallinity, but there is generally expected to be a coupling even within an isotropic phase, reflecting the relative packing capabilities of different isomeric mixtures. This can, in the extreme case, lead to a liquid−liquid phase transition below a critical "spinodal" temperature T_S, with one liquid denser and more conformationally homogeneous than the other. The dense liquid is closer in density and conformation to the crystal phase than the original melt and would thus be expected to have a lower energy barrier Δ to crystallization, with Δ decreasing with increasing quench depth below T_S.

A number of papers[22,23] have been explicitly critical of the spinodal hypothesis[11] and associated experimental studies,[1−10] favoring the traditional picture of nucleation and growth. The argument proposed[22,23] is that the lag between the intensity increase in the SAXS region and the appearance of diffraction peaks in the WAXS region are due to an initial low concentration of small crystals (with a large Debye−Scherrer peak width) having too low an intensity for the WAXS detectors to measure above the background of the amorphous halo, while the more sensitive SAXS detectors, with an increased solid angle of detection with respect to WAXS, can distinguish the crystallite signals. In this work we shall show that the lag is not due to detector sensitivity and that the emergence of Bragg peaks indicates the end of the induction period. The growth of the SAXS intensity in the induction period indicates the evolution of noncrystalline structure. Hsiao et al.[22] report the simultaneous growth of SAXS and WAXS peaks in melt crystallized poly(ether ether ketone) (PEEK), though they noted that this might be due to experimental limits on time resolution. In later work,[23] however, they compare their experimental results on iPP with the results of Ryan et al.[9,10] on iPP, arguing that detector sensitivity is responsible for the time delay and that the predictions of nucleation and growth, more specifically Avrami kinetics, can account for all the features observed. One of their conclusions[23] was that spinodal-assisted crystallization is an inappropriate model and as a consequence was not applied to the new data. Here we use a newly developed WAXS detector with a factor of 10^4 improvement in count rate capabilities over that used in previous experiments in order to test the argument that detector sensitivity is responsible for the delay of WAXS.

There is obviously some debate[24] on whether nucleation and growth alone explains crystallization or whether some precursor phase mechanism may also play a part. Clearly, the mechanism for the early stages of polymer crystallization is an area of considerable controversy, and the conflicting results and interpretations show that there is more work to be done. In accounting for the discrepancies, two issues are worth noting: first, a single system may exhibit either nucleation and growth or spinodal-like kinetics, depending on the depth of the temperature quench, as shown in work on the order−disorder transition in polystyrene−polyisoprene block copolymers.[25] Second, the direction of the shift in SAXS intensity peak position (q_m) may not suffice to confirm or rule out spinodal kinetics. The shift to lower q_m in Cahn−Hilliard theory follows from a model in which the order parameter (concentration in the case of a mixture) is conserved. However, the emergence of nematic order involves a nonconserved order parameter (degree of orientation) coupled to the conserved density, so other models for the hydrodynamics may be more appropriate,[12] although such an analysis will not be addressed in this paper. We report here the detailed studies of the early stages of crystallization in iPP by SAXS/WAXS/DSC techniques using a vastly improved WAXS detector system and compare the results to those reported previously on the early stages of crystallization in iPP.[9,10,23]

Table 1. GPC and DSC Characterization for Samples of IPP

sample	M_w/kg mol^{-1}	M_n/kg mol^{-1}	M_w/M_n	T_m/°C	T_c/°C
Daplen	622	114	5.5	163	99
Finapro	442	93	4.8	165	99
Borealis	267	43	6.2	164	112

Experimental Techniques

Materials. Commercial samples of isotactic polypropylene (iPP) were obtained from PCD Polymer GmbH (Daplen iPP), Fina Chemicals (Finapro iPP), and the Borealis Group (Borealis iPP). High-temperature GPC, in 1,2-dichlorobenzene at 140 °C was employed to obtain molecular weight and distribution measurements against polystyrene standards via the RAPRA Technology Ltd. service (Table 1). Melting and crystal-

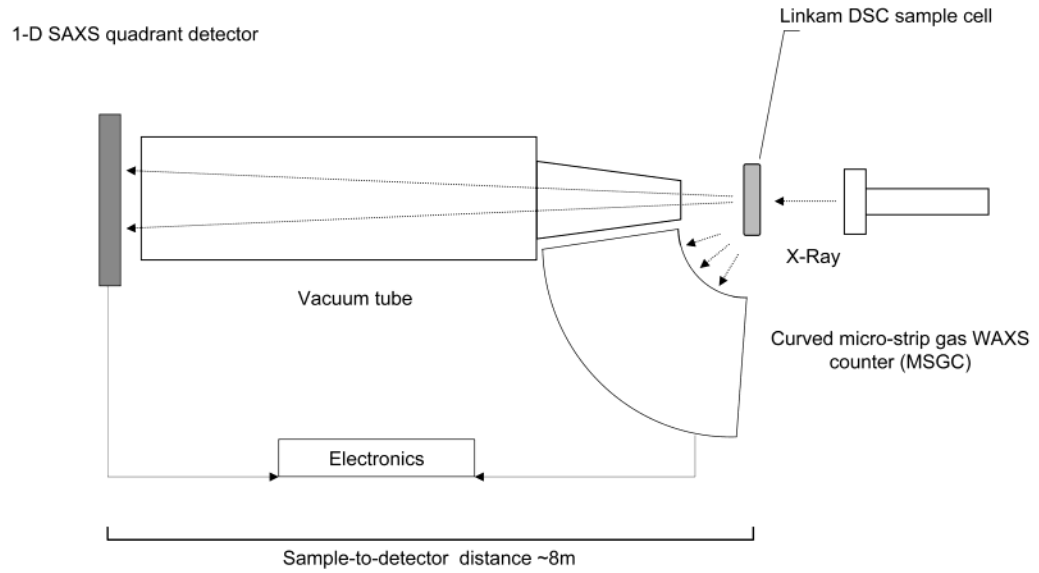

Figure 1. SAXS/WAXS experimental setup on BM26B Dubble beamline at the ESRF, France.

lization temperatures were determined using a Perkin-Elmer Pyris 1 DSC calibrated by the melting points of indium and cyclohexane standards. Samples of mass 5−10 mg, in aluminum pans, were subjected to heating and cooling ramps from 25 to 180 °C at 20 °C/min. All melting and crystallization temperatures were obtained from the peaks of the endotherms and exotherms, during programmed heating and cooling, respectively, using the Pyris DSC software.

X-ray Scattering Measurements. Time-resolved SAXS and WAXS experiments were performed at the Dubble BM26B beamline of the European Synchrotron Radiation Facility (ESRF), Grenoble, France. The ESRF beamline optics and construction are detailed elsewhere.[26] For comparison, similar SAXS/WAXS experiments were performed on station 8.2 at the Daresbury SRS, UK, and the station specifications have been detailed elsewhere previously.[27] The ESRF Dubble beamline operates at variable wavelengths, and for this study a wavelength $\lambda = 1.03$ Å was used. The SAXS detector is situated 8 m from the sample position, and the WAXS data are detected using a newly developed 1D microstrip gas chamber (MSGC) detector system.[26,28,29] A vacuum chamber is placed between the sample and SAXS detector to reduce air scattering and absorption (Figure 1).

Disk-shaped samples of iPP (∼1 mm thickness, ∼8 mm diameter) were housed in aluminum DSC pans supplied by TA Instruments, complete with mica windows (∼25 μm thickness, ∼7 mm diameter).[30] The pans were placed into a single-pan Linkam DSC instrument, whose design and calibration have been previously reported.[31] Samples were heated from 25 to 180 °C at a rate of 20 °C/min and held at this temperature for 5 min; the samples were subsequently quenched at 50 °C/min to the isothermal crystallization temperature T_i and held for up to several hours depending upon T_i. The T_i were in the range $T_c < T_i < T_m$, where T_c is the crystallization maximum during cooling at 20 °C/min and T_m is the melting maximum heating at 20 °C/min. Figure 2 shows a schematic of the DSC heating and cooling procedure, with $t = 0$ indicating the beginning of data collection.

Simultaneous SAXS/WAXS/DSC measurements were obtained for each isothermal crystallization temperature using the Linkam DSC. The X-ray data acquisition was collected at 8 s per frame, with each frame separated by 10 μs wait time. The scattering vector axis, q, of the SAXS patterns were calibrated using an oriented sample of rat-tail collagen, while for the angular calibration of the WAXS patterns HDPE and NBS (National Bureau of Standards) silicon were used. The WAXS intensity data are presented on a 2θ scale renormalized to Cu Kα ($\lambda = 1.54$ Å) radiation.

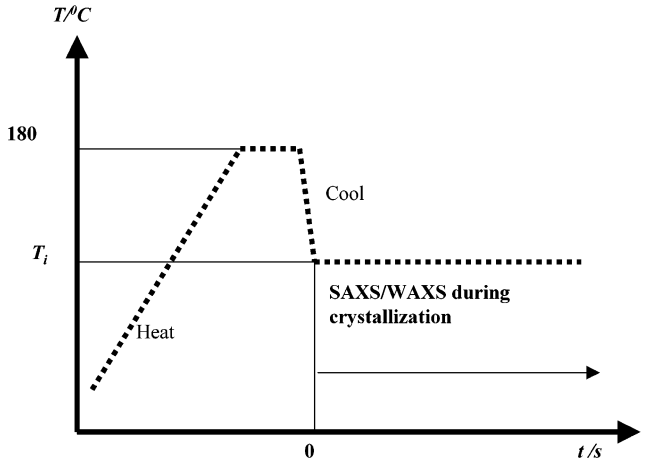

Figure 2. DSC heating and quenching procedure for iPP samples.

Detector Instrumentation. The data from two WAXS detectors are compared herein for a newly developed MSGC WAXS detector at the Dubble beamline with the standard curved linear detector (Inel) used for previous time-resolved SAXS/WAXS experiments at the Daresbury Synchrotron Radiation Source (SRS). The MSGC detector is a fast, efficient, and low noise level instrument, with increased spatial resolution compared to that of wire photon counting detectors. Both the new MSGC and Inel detectors are gas proportional photon counters with essentially similar quantum detection efficiency. However, the real advantage of the MSGC detector system is that it can operate at considerably higher count rates[29] mainly due to the key principle of signal readout; that is, each detector channel is individually equipped with its own readout electronics tracks/circuit, and the design of the detecting elements is such that space charge clouds, which are detrimental to high count rate operation, are reduced by several orders of magnitude compared to the Inel. The use of the MSGC detector technology greatly improves the statistical quality of WAXS data, since the instrument may now be operated essentially at full flux without the need to attenuate the detector. A comparison of the technical specifications of these detectors systems is given in Table 2, detailing the differences in local and global count rate capabilities.

Data Analysis. The SAXS and WAXS data were corrected for background scattering by subtracting contributions from the camera and hot stage and for any detector spatial distor-

Table 2. Comparison of the MSGC and Inel WAXS Detector Systems

detector	focal distance/m	count rate, Cs/s/channel	dynamic range	spatial resolution/μm	global count rate
Inel CPS120, (SRS)	0.25	1×10^3	10^5	500	40 kHz
MSGC, (Dubble)	0.38	4.5×10^5	10^6	200	450 MHz

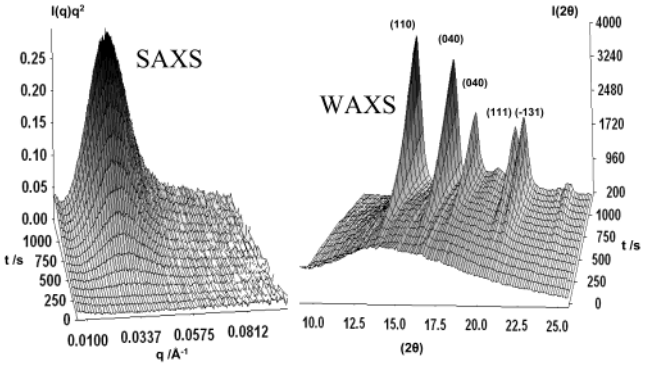

Figure 3. SAXS/WAXS development during isothermal crystallization of Daplen iPP at 130 °C. The WAXS data are presented in 2θ renormalized to Cu Kα ($\lambda = 1.54$ Å).

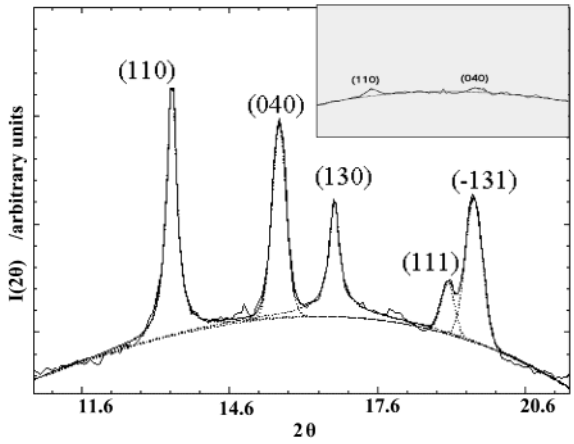

Figure 4. Fitting of WAXS data using a Pearson VII function for the Bragg peaks superimposed on a polynomial background. The inset gives a scattering pattern taken very early in the crystallization process, where the only (110) and (040) peaks are fitted.

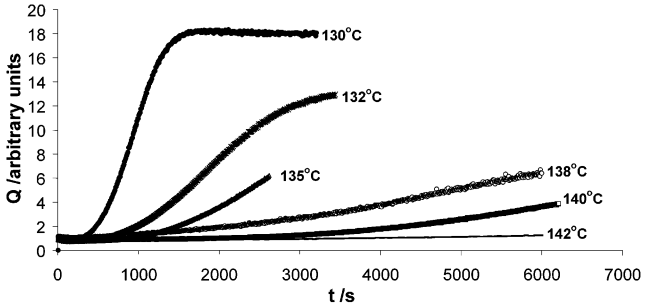

Figure 5. Isothermal crystallization of Daplen iPP at several temperatures shown by the development of the invariant Q, calculated from the SAXS data.

tion. The SAXS data were also corrected for any excess scattering from large inclusions by subtracting the homogeneous melt background taken at 180 °C. Sample thickness and transmission are corrected for by using signals from two parallel-plate ionization chambers placed before and after the sample cell.

Data were reduced to intensity I as a function of scattering vector $q = ((4\pi/\lambda) \sin \theta/2)$, where θ is the scattering angle, using the CCP13 software program, XOTOKO.[32] The SAXS and WAXS data during the crystallization of Daplen iPP at 130 °C are illustrated as three-dimensional plots in Figure 3, corresponding to the Lorentz-corrected SAXS intensity $q^2I(q,t)$ and WAXS intensity $I(2\theta,t)$. The characteristic length $L = 2\pi/q_m$ was determined from the SAXS data using the maximum q_m of $I(q,t)$. At late times this length corresponds to the long period L_p of the semicrystalline structure. In Figure 3, full crystallization at 130 °C gives a final $L_p = 190$ Å.

To show the development of SAXS vs WAXS in the early stages of the iPP crystallization, the relative invariant derived from the SAXS data and the integrated intensity of the crystalline peaks in the WAXS data can be compared to each other. The SAXS relative invariant, Q_S, is defined by

$$Q_S(t) = \int_0^\infty q^2 I(q,t)\, dq \approx \int_{q_1}^{q_2} q^2 I(q,t)\, dq \qquad (1)$$

The relative invariant was obtained by integrating between the experimentally accessible limits, where q_1 and q_1 are respectively the first and the last reliable data points. For all the data discussed here $q_1 = 0.008$ Å^{-1} and $q_2 = 0.09$ Å^{-1} are used consistently throughout the data analysis process. The WAXS crystalline peaks were fitted to a Pearson VII function superimposed on a polynomial background, using the CCP13 program XFIT.[33] Fitting includes the crystalline reflections of the α-monoclinic form of iPP (110, 040, 130, 111, 131) on an amorphous background. Figure 4 shows an example of this fitting procedure for a WAXS pattern from a sample with high crystallinity with five obvious Bragg peaks, whereas the inset gives an early WAXS pattern showing the (110) and (040) peaks during fitting.

The peak parameters (fwhm, integrated peak area, position, and shape) were iteratively refined for each scattering pattern to achieve best fit. The fitting process was performed in reverse order; that is, the most crystalline scattering patterns were fitted first and the parameters from the previous fit then used as the starting point for the current scattering pattern, until all the Bragg peaks disappeared, leaving only the amorphous background. The WAXS crystallinity was obtained by summation of the integrated areas of the Bragg peaks and dividing by the total area under the WAXS curve.

The time evolution of the SAXS invariants for the Daplen iPP is shown in Figure 5 for a range of crystallization temperatures. These plots of quiescent crystallization kinetics clearly show fast crystallization at deep quench temperatures, while much slower crystallization (up to several hours) is seen for the shallow quenches from the melt.

The SAXS invariants and WAXS crystallinity for Daplen iPP crystallized at $T = 130$ °C are shown in Figure 6. The inset is a comparison to the Avrami model,[34] which takes the general form

$$1 - X_s = e^{-kt^n} \qquad (2)$$

where k is the rate constant of the crystallization process, X_s is the crystallinity defined by $X_s(t) = X_W(t)/X_W(\infty)$ (where X_W is the normalized crystallinity from the SAXS invariant), and n is the Avrami exponent which, under certain assumptions, provides information about the dimension of the growing crystalline material. The inset to Figure 6 shows an exponent $n = 3.4$, suggesting spherulitic growth. Deviations from Avrami kinetics, including nonexponential kinetics or noninteger values for n, are often found and can indicate the contemporaneous growth of different types of crystalline units; however, there is currently no consistent theory for such deviations. In Figure 6, a slow nonlinear increase in crystallinity can be seen from both the SAXS and WAXS data at long

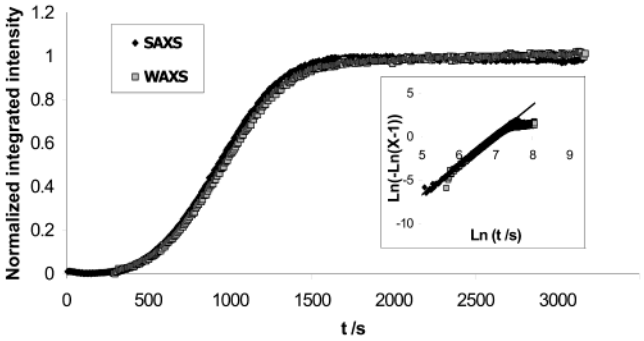

Figure 6. Integrated intensity data from SAXS/WAXS measurements during isothermal crystallization of Daplen iPP at 130 °C. The inset illustrates the Avrami plot of the crystallization where the fit has a slope corresponding to the Avrami exponent $n = 3.4$.

times, which can be ascribed to secondary crystallization, either of a less crystallizable component or the increase in the perfection and/or thickening of the existing crystallites. The description of secondary crystallization is generally well understood.[35] In this work, however, we focus on the very earliest stages of crystallization, prior to the establishment of Avrami kinetics, and study the shape of $I(q,t)$ as well as the invariant.

Analogies of Spinodal Decomposition in Polymer Melts?

There is an obvious delay between the appearance of the SAXS intensity and the onset of crystallites as identified by the WAXS Bragg peaks that is beyond the limits of systematic experimental error. This indicates large-scale density fluctuations before the process of crystallization, which could be attributed either to crystallites being too small or too few in number to generate detectable WAXS scattering or to another process that occurs prior to or simultaneously with the nucleation of detectable crystallites. We will discuss the former possibility below and, later in this section, discuss and analyze the possibility of another process that can induce density fluctuations.

As has been suggested by previous studies on PET[1−3] and *i*-PP,[9,10] we have compared the SAXS pattern to that predicted by the Cahn−Hilliard analysis for spinodal decomposition in binary fluids.[36,37] While the comparison to ordinary spinodal decomposition can be formal at best, since, modulo polydispersity, a polymer melt is a single-species system, several features of the scattering are reminiscent of an instability that is coupled to density.

In a binary fluid undergoing a demixing instability ($T < T_s$), fluctuations $\Psi(q)$ in composition grow exponentially, so that the structure factor $I(q,t) = \langle \Psi(q,t) \Psi(-q,t) \rangle$ also grows exponentially, of the form

$$I(q,t) = I_0 e^{2R(q)t} \tag{3}$$

where the growth rate $R(q)$ is given by

$$R(q) = \mu q^2 \left[a(T_s - T) - \frac{1}{2} g q^2 \right]$$

$$= -q^2 D_{\text{eff}} \left[1 - \frac{1}{2} \left(\frac{q^2}{q_m^2} \right) \right] \tag{4}$$

and I_0 is the initial scattering intensity. Here, μ is the mobility for concentration fluctuations, $-a(T_s - T)$ is the osmotic modulus, which is negative and thus unstable below a certain "spinodal" temperature T_s, and g penalizes composition gradients. The growth rate has a peak at finite $q = q_m = ([a(T_s - T)]/g)^{1/2}$ due to the competition between slow growth at long wavelengths and high energy cost at small wavelengths. The inverse of this wave vector is the typical length scale of the phase separating structure. Conventionally, the structure factor is fitted to an effective diffusion coefficient $D_{\text{eff}} \equiv -\mu a(T_s - T)$ that becomes negative, hence signifying unstable growth, below the spinodal temperature. In conventional binary fluid phase separation at fixed average composition, a typically bicontinuous structure emerges at early times with a constant characteristic length scale until nonexponential (nonlinear) growth is reached, at which point the structure coarsens, the kinetics slows, and eventually a macroscopically phase-separated state is attained. In a polymer melt, however, there is apparently a single species, so any spinodal-like behavior must necessarily be of different origin. Possibilities include the following:

1. A demixing instability induced purely by polydispersity in one of a number of different quantities, such as branching, steroregularity, or molecular weight, which is coupled to density. For example, length polydispersity would lead to regions with longer chains and hence fewer chain ends and, correspondingly, a lower or higher mass density, depending on how the local end density influences packing.

2. A liquid−liquid instability due to the coupling of the density to other "hidden" internal degrees of freedom, with the most likely candidate being the polymer conformation.[11] Such a coupling has been recently shown to be important for understanding hidden liquid−liquid transitions in supercooled water.[38]

3. A final possibility is an instability to an orientationally ordered state, such as a nematic or smectic precursor phase, within which crystallites nucleate quite quickly. Such an intermediate state would accord with Ostwald's rule of phases,[39] by which phase transformations evolve through a series of increasingly less metastable phases. Such a phase would be reminiscent of the mesophases inferred from experiments on extension and shear-induced crystallization,[41−44] although the identification of these scattering signatures with true thermodynamic phases is still suggestive rather than proven.

Which of these scenarios is reasonable for the iPP melts considered here is not clear. While the polydispersity is quite high, there has been little correlation of, for example, the bulk modulus with polydispersity, which would control whether this could influence density differences in the melt. The equilibrium coexistence of liquids of different densities in a single-component system is possible, under controlled pressure conditions, only at a single pressure for a given temperature. This is the content of the Gibbs phase rule. Hence, it is experimentally unlikely that phase separation in an equilibrium state under controlled pressure conditions would be observed, while it would be easily observed under controlled volume conditions. However, if polydispersity plays a role, then coexistence is possible for a range of pressures (and hence possibly observable under controlled pressure conditions) according to the Gibbs phase rule. Since experiments are only performed under essentially constant pressure, the appearance of a spinodal could only be attributed to a transient process. In this case, the less dense phase would become

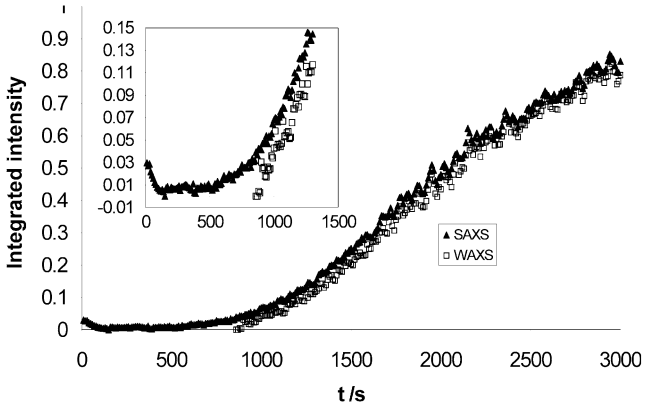

Figure 7. SAXS/WAXS data of isothermal crystallization for Borealis iPP at 140 °C. The inset clearly shows the development of SAXS before WAXS.

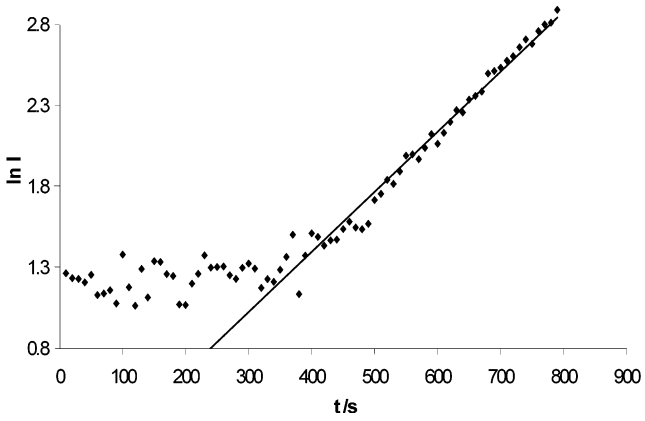

Figure 8. ln I as a function of t from SAXS data for isothermal crystallization of Borealis iPP at 140 °C at a discrete wave vector ($q = 0.0263$ Å^{-1}).

unstable everywhere to the dense phase, at which point a spinodal-like pattern would develop. However, the less dense regions of the spinodal would quickly get squeezed out as the entire system transformed to the dense phase. The relative rates of the growth of the spinodal texture and eventual conversion to the dense phase are controlled by thermal expansion, heat diffusion, viscosity, and the speed of sound.

Recently, Muthukumar and Welch[45] have performed simulations of polymer crystallization from solution and shown that the structure factor resembles that of spinodal decomposition, with a peak position given by balancing crystallization condensation energy against chain stretching energy, and argued that this mechanism could describe the melt-crystallized structure factor. However, this would require an additional mechanism for electron density contrast, and the predicted length scales are much less that the chain dimension, which, as we will see, is incompatible with the much larger length scales observed.

Results

Spinodal Analysis. A Cahn−Hilliard analysis was performed on the induction period of the SAXS data for each iPP sample. This is most relevant for shallow quenches in which an induction period is well-defined. For example in Figure 7, Borealis iPP quenched at 140 °C shows a gap of approximately 500 s between the onset of growth in the SAXS invariant and the detection of Bragg peaks in the WAXS. The developing peak in the SAXS during the early stages of the crystallization has $q_m \approx 0.025$ Å^{-1}, which is commensurate with the final lamellar spacing of order 260 Å.

From the early time SAXS data, we determine the growth rate $R(q)$ from eq 4, fitting $I(q,t)$ to exponential growth for individual wave vectors q. Figure 8 shows ln $I(q,t)$ for a single wave vector at $q = 0.0263$ Å^{-1} for Borealis *i*-PP quenched at 140 °C. The initial flat intensity is essentially the excess scattering caused by the 40 °C drop in temperature as the scattering from a homogeneous melt (at 180 °C) has been subtracted as a background. The growth rate $R(q)$ can be extracted from the data between 400 and 800 s, and Cahn−Hilliard (C−H) plots of $R(q)/q^2$ as a function of q^2constructed, from which the effective diffusion coefficient $D_{eff} \equiv -\mu a(T - T_s)$ can be extracted. Cubic spline functions were fitted to all the SAXS patterns before the C−H analysis was performed, as shown in Figure 9 along with the spinodal region in the behavior of $I(q,t)$. Corresponding

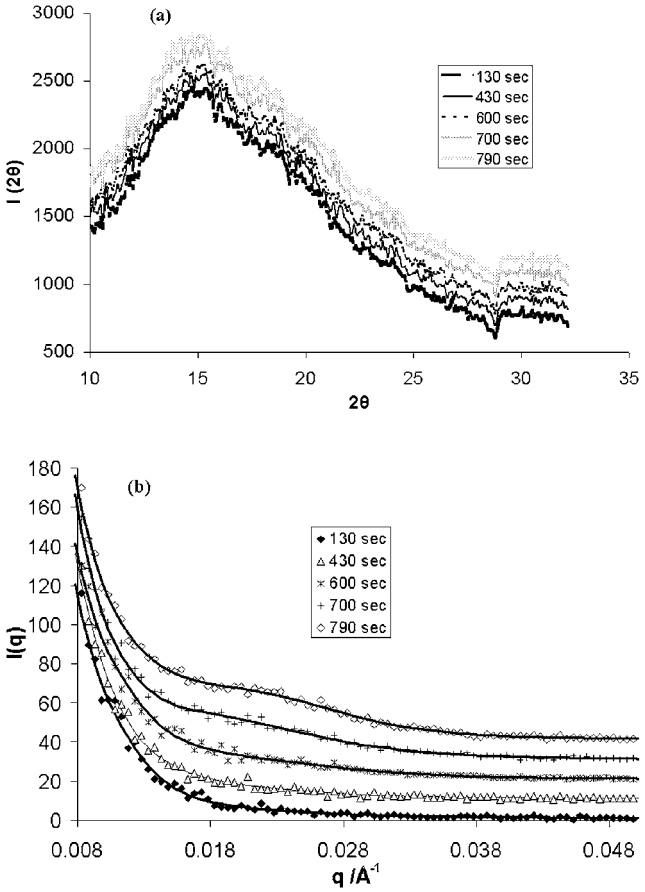

Figure 9. SAXS/WAXS spinodal region for Borealis iPP at 140 °C: (a) selection of WAXS frames; (b) corresponding selection of SAXS data where the solid line corresponds to the cubic spline fit to the data. The intensity data for both SAXS and WAXS successive time frames are offset for clarity.

WAXS frames are also plotted in Figure 9, showing the lack of any early Bragg peaks during this period.

To extract D_{eff}, a straight line was fitted to $R(q)/q^2$ given in standard C−H analysis by $q_m < q < \sqrt{2}q_m$. At the upper limit higher order terms in q preempt the simplified form, and at the lower limit the data are typically influenced by excess scattering. The C−H plot for Borealis iPP at 140 °C is shown in Figure 10 and for a range of temperatures for Daplen, Finapro, and Borealis in Figure 11. From D_{eff} determined at several quench temperatures (Figure 11), it is possible to

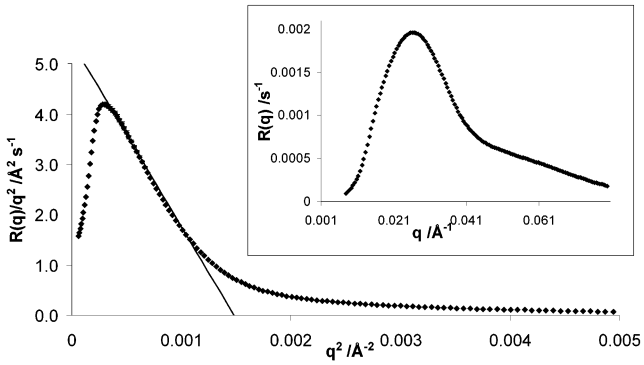

Figure 10. C−H plot of Borealis iPP at 140 °C. From the solid line fit, D_{eff} is estimated from the intercept $q = 0$. Inset: $R(q)$ vs q. The errors propagated from the raw data through the analysis procedure give error bars such that they are of similar size to the plot points.

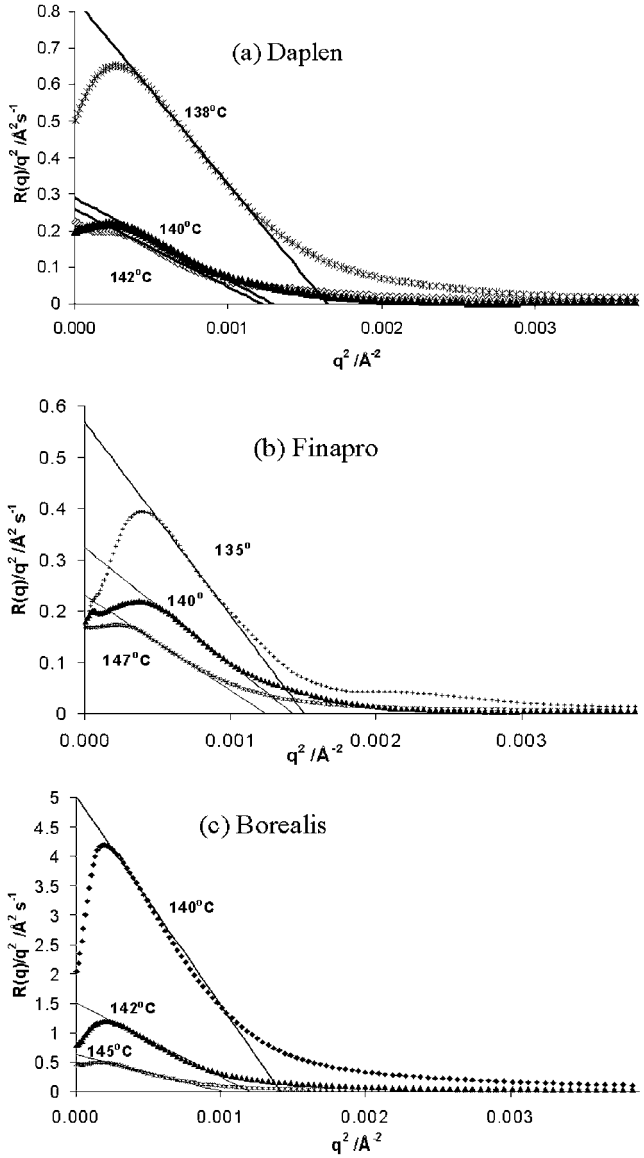

Figure 11. Selection of C−H plots where the extrapolation of the straight-line portion of the graph gives rise to the D_{eff} values at each specific temperature: (a) Daplen iPP, (b) Finapro iPP, and (c) Borealis iPP.

extrapolate to determine an effective spinodal temperature T_s, which, if C−H analysis applies, corresponds to the lower limit of stability of the melt.

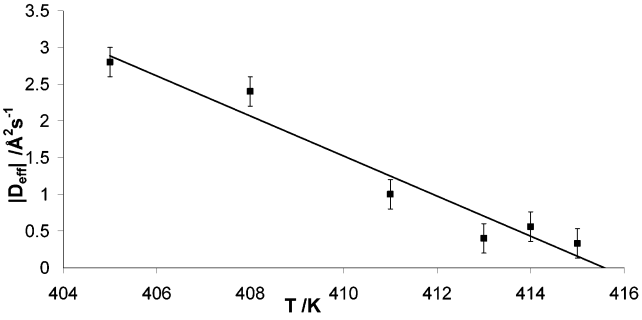

Figure 12. (a) Plot of $|D_{eff}|$ vs T for the Daplen iPP sample. The spinodal temperature T_s is calculated by extrapolating to $D_{eff} = 0$.

Table 3. Details of Spinodal Temperatures for IPP Samples

sample	M_w/kg mol^{-1}	R_g/Å[b]	T_s/K	D_{eff}(138 °C)/ Å^2 s^{-1}	q_m(138 °C)/ Å^{-1}
Daplen	622	250	416	−1.0	0.031
Finapro	442	210	419	−1.4	0.031
Borealis	267	164	422	−1.6	0.032
S-30-S[a]	520	226	415	−6.9	−

[a] Values for sample S-30-S were obtained previously from Ryan et al.[10] [b] Values of R_g were calculated from M_w using $R_g = N^{1/2}b$, where b is the statistical segment length of polypropylene.[46]

Figure 12 shows a plot of D_{eff} as a function of T for Daplen iPP to demonstrate the extrapolation to determine the spinodal temperature T_s. These data are collected in Table 3 for the three *i*-PP samples, along with another *i*-PP sample S-30-S[9,10] that was previously studied under similar quiescent crystallization conditions using SAXS/WAXS at the Daresbury SRS. On average, they are similar (except the S-30-S sample), with a value of $D_{eff} \approx -1$ Å^2 s^{-1} at $T = 138$ °C.

The stability limit can be described as the temperature below which the melt spontaneously separates into two phases. The two phases could either be isotropic liquids, with one rich in conformational states more appropriate for crystallization and denser and one depleted of these conformational states and thus less dense. Another possibility is that a transition to a metastable or unstable liquid crystalline phase has occurred (which will also give rise to a spatial density modulation). In either case, the structured melt is evidently unstable to crystallization due to enhanced nucleation. The stability limits of the three iPP samples are given in Table 3 along with data for the S-30-S iPP sample determined from previous data.[10]

From the C−H analysis we find $T_s = 419 \pm 3$ K, which agrees well with the value 415 ± 5 K found previously for S-30-S.[9,10] This is of order 18 K below the measured melting point for iPP crystals with long spacing 175 Å and 40 K below the thermodynamic melting point of iPP, $T_m = 459$ K.[46] Given that there is only a factor of ≈2.3 difference in the molecular weight of the polymers (and a corresponding 1.5 difference in R_g), it is difficult to interpret the differences in D_{eff} and T_s other than to note that they vary systematically with the mobility being directly proportional, and the stability limit being inversely proportional, to the molecular weight.

During the spinodal, or induction, period we can also follow the time evolution of the peak wave vector q_m, shown in Figure 13 for three crystallization temperatures, 140, 142, and 145 °C. It is clear to that q_m is constant or slightly decreasing with time, and the corresponding length scale is greater (q_m is smaller) for

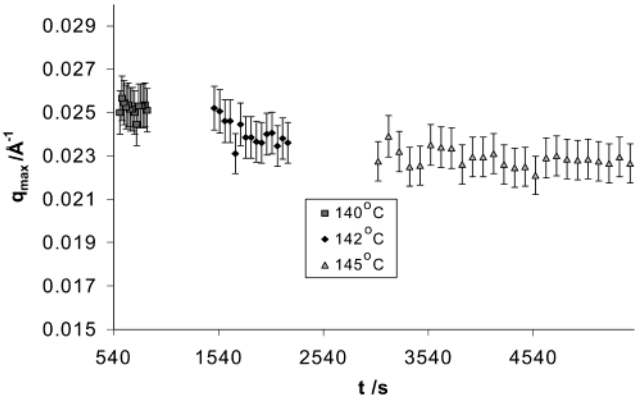

Figure 13. SAXS wave vector peak q^* as a function of time during the spinodal period for Borealis iPP.

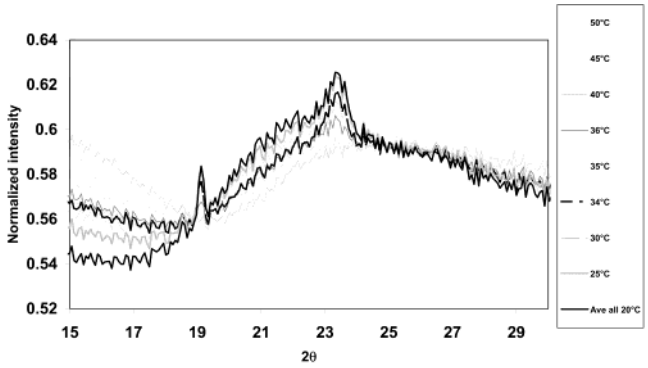

Figure 14. Series of WAXS frames taken over a temperature ramp of a 0.5 wt % $E_{76}B_{38}$ diblock copolymer crystallization in hexane. The crystallization taking place within the micelle core is clearly seen by the emergence of the WAXS Bragg peaks at $2\theta \sim 19°$ and 23.5°.

higher crystallization temperatures. This coarsening of the length scale is observed when phase separation has passed the linear regime and is usually seen in spinodal decomposition of small molecules because of the rather fast growth. In the early stages of spinodal decomposition in entangled polymer blends the principal wavelength can remain constant for some appreciable time, but this is rather unusual behavior.[13] While the early SAXS data are well described by the C−H model, a rigorous analysis of C−H predicts an intensity crossover in the linear regime; that is, a wave vector q_{ic} exists above which the intensity decays and below which the intensity grows, such that the intensity at q_{ic} is unchanged. This is apparent in the original work by Cahn and Hilliard on metals and the seminal studies of the early stages of crystallization by Schultz et al.[47,48] Our data here are not consistent with this predicted behavior, However, we offer two comments about this: (i) When noise is added to the C−H equations (Cahn−Hilliard−Cook), the resulting intensity generated at all wave vectors at all times obscures the "ideal" crossover. Instead, one expects a decay essentially to zero near q_{ic}. (ii) Our system is not definitely in the linear regime; the lack of knowledge of contributions to the nonlinear dynamics (including viscoelastic and density effects) precludes definite predictions about this behavior. The characteristic length scale of the SAXS pattern, $L = 2\pi/q_m$, is ~200 Å, which is of the order of R_g (values quoted in Table 3). This is inconsistent with the mechanism proposed by Muthukumar and Welch,[45] which predicts "baby nuclei" smaller than R_g.

Detector Sensitivity. A common criticism of the spinodal interpretation of the early stages of crystallization is the lack of statistically relevant data and the mismatch between the sensitivity of the SAXS and WAXS techniques toward the events under investigation. The greater sensitivity of SAXS experiments with respect to WAXS experiments, partly related to count rate limitations on the WAXS detectors, would lead to an intrinsic systematic lag between the two signals. To obtain a high data quality, WAXS detectors require a very high local count rate due to the fact that the diffraction features are mapped onto small number of pixels. This in contrast with SAXS experiments which, in general, have the interesting features mapped onto a large part of the active surface of the detector. This overcomes problems with local count rate limitations by integrating a large number of detector pixels. We have addressed this issue by using a newly constructed gas−microstrip WAXS detector system.[29] With this detector the local and sustainability of count rates at are greatly increased (by at least a factor of 400 per pixel), along with improved signal-to-noise ratio, compared with detectors used previously. This has effectively allowed us to obtain WAXS data without compromising the incident flux falling on the detector at high frame rates.

We have recently been able to demonstrate detection of crystallinity in a block copolymer with crystals of overall dimensions <7 nm. The data are shown in Figure 14, which shows unequivocally the growth of crystallinity from a solution with a crystallizable mass of 0.25 wt %. The block copolymer is a poly(ethylene oxide/butylene oxide) diblock copolymer ($E_{76}B_{38}$) at 0.5 wt % in hexane, a preferential solvent for B. We estimate E to be at most 80% crystalline, and the WAXS peaks can be seen to grow as crystallization occurs in the micelle core at $\Delta T \cong 20$ K. This is a reasonable comparative experiment as the ΔT value is commensurate with those studied here, but most importantly the crystallites are small. With the polymers in solvent experiments conducted by others,[50] the crystallites are rather large (typically microns) which would tend to overestimate the detector sensitivity. Using this well-designed experiment, we can actually verify the mass crystallinity detection limit to be 0.05 wt % as we have data through the growth to a final crystallinity of 0.2 wt %. Interestingly, the shape factor of the isolated micelles also changes during crystallization, and this will be reported elsewhere. Of course, the diblock copolymer system contains oxygen, and so there is a corresponding increase in the scattering cross section; however, this would bring the detection up to 0.1 wt % for a polyolefin. We recognize that the same experiments need to be conducted with a block copolymer having an iPP crystallizable block and are working on the synthesis of such a polymer.

It is important that the issue of diffraction peak intensity as a function of temperature is addressed.[51,52] The model diblock copolymer system here has the same ΔT as the polypropylene, but the absolute crystallization temperature is approximately 100 °C lower. The problem in estimating the effect of thermal broadening is the lack of published Debye temperatures for polymers. Our most generous estimate, using a Debye temperature of 200 K, is that the peak intensity will be decreased by a factor of 2. This will give a further revised estimate of detection limit of 0.2 wt %. Previously, Wang et al.[50] have reported that SAXS detection systems can detect levels of crystallinity as small as ≈0.3% whereas

conventional WAXS detector systems were only able to discern crystallinity an order of magnitude above this for large crystals. Our final detection limit of 0.2 wt % is thus still smaller than the detection limit of SAXS estimated by Wang with this newly developed WAXS instrumentation and data discussed here.

Conclusions

Slow crystallization of several iPP samples has been studied with simultaneous SAXS/WAXS techniques. Previously, similar crystallization data were reported for *i*-PP[9,10,23,50] and PET.[1−3] An initial SAXS pattern that develops prior to the WAXS Bragg reflections was analyzed in the context of density fluctuations which are reminiscent of spinodal decomposition in binary fluids, and the applicability of this picture to polymer melts has been discussed.

The improved detector count rate capabilities of the WAXS detector system reported here allow the SAXS and WAXS detection limits to be comparable. Still we observe SAXS intensity growing for hundreds of seconds before crystalline reflections are present in the WAXS at shallow quench depths. This is despite a factor of 10^4 increase in the global count rate of the new MSGC WAXS detector instrumentation compared to previous experiments. The SAXS data for three different samples of iPP have been analyzed in the framework of the Cahn−Hilliard theory for spinodal decomposition. During the development of the SAXS peak (prior to WAXS), the effective diffusion coefficient has been measured for several quench temperatures for each sample. This has thus enabled an estimate of the spinodal temperature to be obtained in each case. Generally, the spinodal temperatures are comparable for each iPP sample. The earlier data for a similar iPP sample (S-30-S) also give similar results when calculating T_s using the C−H analysis. One difference that is apparent, however, is that the gap between SAXS and WAXS in earlier data[9,10] was observed to be greater at deeper quench depths compared with the data here. We conclude, therefore, that detector limitations could account for this discrepancy in our earlier data, as crystallinity in the WAXS was not detected at lower levels. In the present work deeper quench depths, where the crystallization rate is increased, gave reduced gaps between SAXS and WAXS or none at all, verifying the improved detector sensitivity.

Clearly, in earlier reports and in the present work, the gap between the SAXS intensity and the WAXS intensity during crystallizations from the melt has been confirmed as a characteristic of the early stages of the crystallization. The use of improved detector systems has reduced limitations in detecting the WAXS signal, and still the gap is observed. That there is a qualitative difference between the crystallization behavior at shallow undercooling and that at large undercooling is beyond experimental doubt. At $T_s - T = 1$ K there is a 50 min period of evolution of a peak in the SAXS intensity with no measurable change in the WAXS. In contrast, at $T_s - T = 20$ K scattering is observed contemporaneously in both the SAXS and WAXS regimes and can be fitted to Avrami kinetics throughout.

What causes this qualitative difference in the crystallization behavior? At low T, the crystallization behavior is clearly heterogeneously nucleated from the beginning. At high T, there is little evidence of homogeneous nucleation phenomena. Here, Ostwald's rule of stages[39] seems to apply, and a metastable, low order phase precedes the formation of the equilibrium crystal structure. Reprising the possible causes of this qualitative difference, one can easily disregard polydispersity effects as they are of vanishingly small magnitude. The coupling of density and polymer conformation to give a liquid−liquid instability is attractive and has been suggested by Olmsted et al.[11] An instability to an orientationally ordered state is also suggestive, and ongoing studies of the effect of flow on crystallization kinetics favor this argument.

Acknowledgment. E.L.H. was supported from the EPSRC Microscale Polymer Processing project (GR/M60415) which also provided beamtime at the Daresbury SRS. The beamtime at the ESRF was provided under the LTP SC 777. The authors are grateful for the assistance of the ESRF Dubble-CRG and the Daresbury SRS beamline staff. The polymers were kindly provided by PCD Polymer GmbH, Fina Chemicals, and the Borealis group. Dr. Xu Junting kindly provided the data for Figure 14 in advance of its publication.

References and Notes

(1) Imai, M.; Mori, K.; Mizukami, T.; Kaji, K.; Kanaya, T. *Polymer* **1992**, *33*, 4451.
(2) Imai, M.; Mori, K.; Mizukami, T.; Kaji, K.; Kanaya, T. *Polymer* **1992**, *33*, 4457.
(3) Imai, M.; Kaji, K.; Kanaya, T. *Macromolecules* **1994**, *27*, 7103.
(4) Nogales, A.; Ezquerra, T. A.; Denchev, Z.; Sics, I.; Balta Calleja, F. J.; Hsiao, B. S. *Chem. Phys.* **2001**, *115*, 3804.
(5) Matsuba, G.; Kaji, K.; Nishida, K.; Kanaya, T.; Imai, M. *Polym. J.* **1999**, *31*, 722.
(6) Matsuba, G.; Kaji, K.; Nishida, K.; Kanaya, T.; Imai, M. *Macromolecules* **1999**, *32*, 8932.
(7) Matsuba, G.; Kanaya, T.; Saito, M.; Kaji, K.; Nishida, K. *Phys. Rev. E* **2000**, *62*, 1497.
(8) Ezquerra, T. A.; Lopez-Cabarcos, E.; Hsiao, B. S.; Balta-Calleja, F. H. *Phys. Rev. E* **1996**, *54*, 989.
(9) Terrill, N. J.; Fairclough. P. A.; Towns-Andrews, E.; Komanschek, B. U.; Young, R. J.; Ryan, A. J. *Polymer* **1998**, *39*, 2381.
(10) Ryan, A. J.; Fairclough. P. A.; Terrill, N. J.; Olmsted, P. D.; Poon, W. C. K. *Faraday Discuss.* **1999**, *112*, 13.
(11) Olmsted, P. D.; Poon, W. C. K.; McLeish, T. C. B.; Terrill, N. J.; Ryan, A. J. *Phys. Rev. Lett.* **1998**, *81*, 373.
(12) Chaikin, P. M.; Lubensky, T. C. *Principles of Condensed Matter Physics*; Cambridge University Press: Cambridge, MA, 1995.
(13) Bates, F. S.; Wiltzius, P. *J. Chem. Phys.* **1989**, *91*, 3258.
(14) Balta-Calleja, F. J. Proceedings of the "International Symposium on Polymer Crystallisation", June 9−12, 2002, Mishima, Shizuoka, Japan.
(15) Blundell, D. J.; MacKerron, D. H.; Fuller, W.; Mahendrasingam, A.; Martin, C.; Oldman, R. J.; Rule, R. J. Riekel, C. *Polymer* **1996**, *37*, 3303.
(16) Welsh, G. E.; Blundell, D. J.; Windle, A. H. *Macromolecules* **1998**, *31*, 7562.
(17) Tashiro, K.; Sasaki, S.; Kobayashi, M. *Macromolecules* **1996**, *29*, 7460.
(18) Tashiro, K.; Sasaki, S.; Gose, N.; Kobayashi, M. *Polym. J.* **1998**, *30*, 85.
(19) Sasaki, S.; Tashiro, K.; Kobayashi, M.; Izumi, Y.; Kobajashi, M. *Polymer* **1999**, *40*, 7125.
(20) Huang, J.-M.; Chu, P. P.; Chang, F.-C. *Polymer* **2000**, *41*, 1741.
(21) Doi, M.; Shimada, T.; Okano, K. *J. Chem. Phys.* **1988**, *88*, 4070.
(22) Hsiao, B. S.; Sauer, B. B.; Verma, R. K.; Zachman, G. H.; Seifert, S.; Chu, B.; Harney, P. *Macromolecules* **1995**, *28*, 6931.
(23) Wang, W.; Schultz, J. M.; Hsiao, B. S. *Macromolecules* **1997**, *30*, 4544.
(24) Strobl, G *Eur. Phys. J. E*: *Soft Matter* **2000**, *3*, 165−183. Lotz, B. *Eur. Phys. J. E*: *Soft Matter* **2000**, *3*, 185−194. Cheng, S. Z. D.; Li, C. Y.; Zhu, L. *Eur. Phys. J. E*: *Soft Matter* **2000**, *3*, 195−197. Muthukumar, M. *Eur. Phys. J. E*: *Soft Matter* **2000**, *3*, 199−202.

(25) Balsara, N. P.; Garetz, B. A.; Newstein, M. C.; Bauer, B. J.; Prosa, T. J.; *Macromolecules* **1998**, *31*, 7668.
(26) Bras, W. *J. Macromol. Sci., Phys.* **1998**, *B37*, 557.
(27) Bras, W.; Derbyshire, G. E.; Ryan, A. J.; Mant, G. R.; Felton, A.; Lewis, R. A.; Hall, C. J.; Greaves, G. N. *Nucl. Instrum. Methods Phys. Res.* **1993**, *A326*, 587.
(28) Zhukov, V.; Udo, F.; Marchena, O.; Hartjes, F. G.; van den Berg. F. D.; Bras, W.; Vlieg, E. *Nucl. Instrum. Methods Phys. Res.* **1997**, *A392*, 83.
(29) Dolbnya, I. P.; Alberda, H.; Hartjes, F. G.; Udo, F.; Bakker, R. E.; Konijnenburg, M.; Homan, E.; Cerjak, I.; Goedtkindt, P. *Rev. Sci. Instrum.* **2002**, *11*, 3754.
(30) Ryan, A. J. *J. Therm. Anal.* **1993**, *40*, 887.
(31) Bras, W.; Derbyshire, G. E.; Mant, G. R.; Clarke, S. M.; Cooke, J.; Komanschek, B. U.; Ryan, A. J. *J. Appl. Crystallogr.* **1994**, *28*, 26.
(32) http://www.srs.dl.ac.uk/ncd/computing/manual.otoko.html.
(33) Hamley, I. W.; Denny, R. C.; Matsen, M.; Liao, B.; Booth, C.; Ryan, A. J. *Macromolecules* **1997**, *38*, 509.
(34) Avrami, M. *J. Chem. Phys.* **1939**, *7*, 1103; *J. Chem. Phys.* **1940**, *8*, 212.
(35) Marand, H. Alizadeh, A. *Polym. Mater. Sci. Eng.* **1999**, *81*, 238.
(36) Cahn, J. W.; Hilliard, J. E. *J. Chem. Phys.* **1958**, *28*, 25.
(37) Gunton, J. D.; San Miguel, M.; Sahni, P. S. In *Phase Transitions and Critical Phenomena*; Domb, C., Green, M. S., Eds.; Academic: New York, 1983; Vol. 8.
(38) Yamada, M.; Mossa, S.; Stanley, E.; Sciortino, F. *Phys. Rev. Lett.* **2002**, *88*, 195701.
(39) Ostwald, W. *Z. Phys. Chem.* (*Munich*) **1897**, *22*, 289.
(40) Blundell, D. J.; Mahendrasingam, A.; Martin, C.; Fuller, W. *J. Mater. Sci.* **2000**, *35*, 5057.
(41) Welsh, G. E.; Blundell, D. J.; Windle, A. H. *J. Mater. Sci.* **2000**, *35*, 5225.
(42) Blundell, D. J.; Mahendrasingam, A.; Martin, C.; Fuller, W.; MacKerron, D. H.; Harvie, J. L.; Oldman, R. J.; Riekel, C. *Polymer* **2000**, *41*, 7793.
(43) Mahendrasingam, A.; Martin, C.; Fuller, W.; Blundell, D. J.; Oldman, R. J.; MacKerron, D. H.; Harvie, J. L.; Riekel, C. *Polymer* **2000**, *41*, 1217.
(44) Welsh, G. E.; Blundell, D. J.; Windle, A. H. *Macromolecules* **1998**, *31*, 7562.
(45) Muthukumar, M.; Welch, P. *Polymer* **2000**, *41*, 8833. Welch, P.; Muthukumar, M. *Phys. Rev. Lett.* **2001**, *87*, 218302.
(46) Mark, J. E. *Physical Properties of Polymers*; American Institute of Physics: New York, 1996.
(47) Schultz, J. M.; Lin, J. S.; Hendricks, R. W. *J. Polym. Sci., Polym. Phys. Ed.* **1981**, *19*, 609.
(48) Babajko, S.; Schultz, J. M. *J. Polym. Sci., Polym. Phys. Ed.* **1982**, *20*, 497. Petermann, J.; Gohil, R. M.; Schultz, J. M.; Hendricks, R. W.; Lin, J. S. *J. Polym. Sci., Polym. Phys. Ed.* **1982**, *20*, 523.
(49) Cernik, R. J.; Bushnell-Wye, G.; Dent', A. J.; Daikun, G. P.; Tang, C. C.; Terrill, N. J.; Flaherty, J. V.; Kay, J.; Barnes, P.; Greaves, G. N.; Rayment, T.; Ryan. A. J. *J. Synchrotron Rad.*, submitted for publication.
(50) Wang, Z. G.; Hsiao, B. S.; Sirota, E. B.; Agarwal, P.; Srinivas, S. *Macromolecules* **2000**, *33*, 678.
(51) Cullity, B. D. *Elements of X-ray Diffraction*, 2nd ed.; Addison-Wesley: London, 1979.
(52) Bras, W.; Dolbnya, I. P.; Detollenaere, D.; van Tol, R.; Malfois, M.; Greaves, G. N.; Ryan, A. J.; Heeley, E. L. *J. Appl. Crystallogr.* **2003**, *36*, 791.

MA021373I